Available online at www.sciencedirect.com

ScienceDirect

Advances in Space Research 68 (2021) 4691–4701

ADVANCES IN SPACE RESEARCH (a COSPAR publication)

www.elsevier.com/locate/asr

Prominent volcanic source of volatiles in the south polar region of the Moon

David A. Kring [a,*], Georgiana Y. Kramer [b], D. Benjamin J. Bussey [c], Dana M. Hurley [c], Angela M. Stickle [c], Carolyn H. van der Bogert [d]

[a] Center for Lunar Science and Exploration, USRA-Lunar and Planetary Institute, 3600 Bay Area Blvd., Houston, TX 77058, United States
[b] Planetary Science Institute, Tucson, AZ, United States
[c] Johns Hopkins University Applied Physics Laboratory, Laurel, MD, United States
[d] Institut für Planetologie, Westfälische Wilhelms-Universität Münster, Wilhelm Klem Str. 10, 48149 Münster, Germany

Received 2 February 2021; received in revised form 19 July 2021; accepted 10 September 2021
Available online 20 September 2021

Abstract

Gas-rich discharges of magma produced pyroclastic vents on the lunar surface. Calculations suggest those pyroclastic vents repeatedly generated 10^{12} to 10^{15} g of H_2O and $CO + CO_2$ for pyroclastic volumes of 10 to 500 km^3 early in lunar history, particularly during the first billion years of lunar history. Some of those volatiles migrated to the lunar poles where they could be trapped in permanently shadowed regions (PSRs). The largest indigenous source of volatiles in the south polar region was volcanism that occurred on the floor of the Schrödinger impact basin. Here a large pyroclastic vent ceased erupting $\sim 3.70\ ^{+0.02}_{-0.03}$ Ga, releasing H_2O, CO-CO_2, F, S, and Cl vapor species, including calculated values of 3.0×10^{13} to 1.6×10^{14} g H_2O. A transport and depositional model suggests 1.1×10^{10} kg (12%) of that water may have been trapped in the south polar region.

1. Introduction

The discovery of measurable quantities of water in lunar samples (Saal et al., 2008; Hauri et al., 2011) prompted a re-evaluation of the volatile inventories on the Moon, including deposits of water and other volatile species preserved in surface and near-surface deposits in permanently shadowed regions (PSRs) that act as cold traps (e.g., Watson et al., 1961; Arnold, 1979; Paige et al., 2010). Because the elemental and isotopic nature of such deposits would provide measures of the indigenous lunar volatile cycle and exogenous contributions from other Solar System reservoirs, the National Research Council (NRC 2007) identified polar deposits as a high-priority science target. Moreover, water-bearing volatile deposits would be an immense resource for space exploration activities, providing material for crew consumption, radiation shielding, and propellants and are, thus, a critical exploration target, too. Landing sites that provide access to volatile deposits and/or the planetary processes that constrain volatile abundances are the current targets of a joint Roscosmos-European Space Agency (ESA) robotic initiative and the National Aeronautics and Space Administration's (NASA's) robotic VIPER mission and its Artemis human exploration program.

The indigenous volatile cycle began with the delivery of volatiles to the lunar interior during the magma ocean phase of lunar evolution (Barnes et al., 2016). A portion of those volatiles were subsequently carried back to the surface by volcanic processes. These volatile-rich eruptions were principally driven by C-O gas phases (e.g., Rutherford and Papale, 2009), although new analyses of Apollo 15 and 17 glasses (Saal et al., 2008; Hauri et al.,

* Corresponding author.
E-mail address: kring@lpi.usra.edu (D.A. Kring).

https://doi.org/10.1016/j.asr.2021.09.008
0273-1177/

2011) suggest H-O species were also involved. Once liberated at the lunar surface, the volatiles would have augmented solar wind volatiles implanted in the regolith (Haskin and Warren, 1991). To assess that volatile contribution, the composition of pyroclastic glasses collected at the Apollo 15 and 17 landing sites are used to calculate the production of volatiles degassed in lunar pyroclastic eruptions of different sizes on the Moon. Here we suggest that pyroclastic vents were capable of repeatedly generating 10^{12} to 10^{15} g of H_2O and CO + CO_2 for pyroclastic volumes of 10 to 500 km^3 during the past ~ 3.7 billion years (Gaddis et al., 2003) and likely earlier in lunar history, although evidence of most older vents has been erased. Older vents may have been generated when mare – now observed as cryptomare (Whitten and Head, 2015) and inferred from gravity (Sori et al., 2016) – with model ages > 3.8 Ga were being emplaced. Basalt with radiometric U-Pb eruption ages > 4 Ga have also been detected in lunar meteorite MIL 13,317 (Shaulis et al., 2016; Snape et al., 2018). Fumarolic activity in the lunar highlands was inferred > 3.8 Ga based on enrichment of volatile elements (Krähenbühl et al., 1973) and may have been responsible for the oxidative formation of magnetite in ancient regolith breccia 66016 (Joy et al., 2015).

Each one of those observed and inferred vents may have produced orders of magnitude more mass than exists in the current lunar exosphere (2×10^7 g) (Stern, 1999). The Schrödinger vent is the only vent in the south polar region, so it may be the dominant indigenous source of any polar volatile deposits after the basin-forming epoch.

Because of the in situ resource utilization (ISRU) potential of volatile elements, an immense ~ 400 m-tall pyroclastic deposit in the Schrödinger basin was among the Tier I and II targets during NASA's Exploration Systems Mission Directorate (ESMD)-phase of the Lunar Reconnaissance Orbiter (LRO) mission and a NASA Constellation Program Office Region of Interest (e.g., Keller et al., 2016). Both robotic (Potts et al., 2015; Steenstra et al., 2016) and human (O'Sullivan et al., 2011; Bunte et al., 2011; Burns et al., 2013; Allender et al., 2019) missions are envisioned for that location. The Schrödinger impact melt, potentially near the pyroclastic vent, is the target for a 2024 robotic lander in NASA's Commercial Lunar Payload Services (CLPS) program.

Because the Schrödinger basin is an exploration target and the vent within it a source of volatile elements that may be enountered at other landing sites, we provide a case study of the Schrödinger pyroclastic vent. A transport and depositional model, discussed herein, indicates substantial fractions of the volatiles emitted from that vent would have been trapped in PSRs across the region and closer to the pole. We note that another high priority NRC (2007) objective is to investigate the transport and deposition of volatiles in the polar regions of the Moon. This vent provides an "experiment" – producing a geographical and temporal point source of material that can be traced towards the lunar poles to test transport and depositional

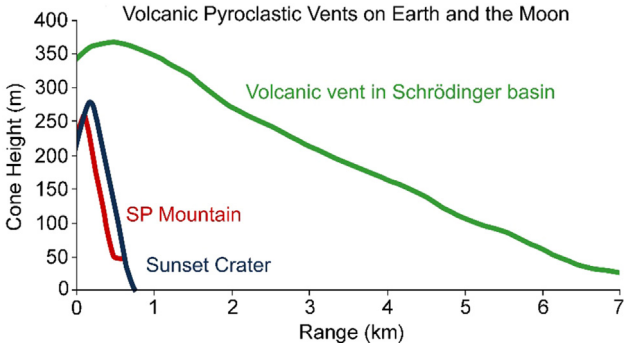

Fig. 1. Comparison of the topographical profiles of the pyroclastic vent in the Schrödinger basin and two lunar analogue vents on Earth. The centers of the cones are along the vertical axis. Terrestrial cinder cones are generally < 100 m high, although rarely they may reach a height of 450 m (Settle, 1979).

models. This vent is among the 'large' vent deposits catalogued on the Moon (Gaddis et al., 2003), in this case covering an area of 819 km^3 (Gaddis et al., 2003), and is immense compared with terrestrial analogues SP Mountain and Sunset Crater (Fig. 1), two cinder cones in northern Arizona that are used for astronaut training and lunar mission simulations.

2. Methods

Vent age. To determine the age of the Schrödinger vent, we made a crater size-frequency distribution (CSFD) measurement on the northwest side of the vent (Fig. 2a) and fit the data to derive an absolute model age. We used the SELENE Terrain Camera seamless orthomosaic (~7 m/px resolution; Haruyama et al., 2008) for crater measurements in ArcGIS via the CraterTools Add-In (Kneissl et al., 2011), following the approach of Neukum (1983), Neukum et al. (2001), Hiesinger et al. (2011), and references therein. A slope map derived from a 60 m/pixel Lunar Orbiter Laser Altimeter (LOLA) digital elevation model (DEM) (Smith et al., 2010) was used to select a count area without significant slopes (<5° with patches of < 10°, except for small crater walls), because downslope mass wasting can alter the CSFDs of small craters (e.g., van der Bogert et al., 2018; Basilevsky, 1976). Because the method relies on the measurement of all primary craters in a homogeneous region of a single geological unit, areas with obvious secondary craters, including chains and clusters, were excluded from the defined count area. The resulting CSFD was fit with the Neukum et al. (2001) lunar production and chronology functions, which is valid for craters with diameters of 10 m to 100 km, using Poisson timing analysis (Michael et al., 2016) to give an absolute model age for the pyroclastic unit.

Volume of pyroclastic eruption. The pyroclastic vent erupted onto the Schrödinger basin floor. The topography of the vent on top of that horizon is extracted from Lunar Orbiter Laser Altimeter (LOLA) data and divided into

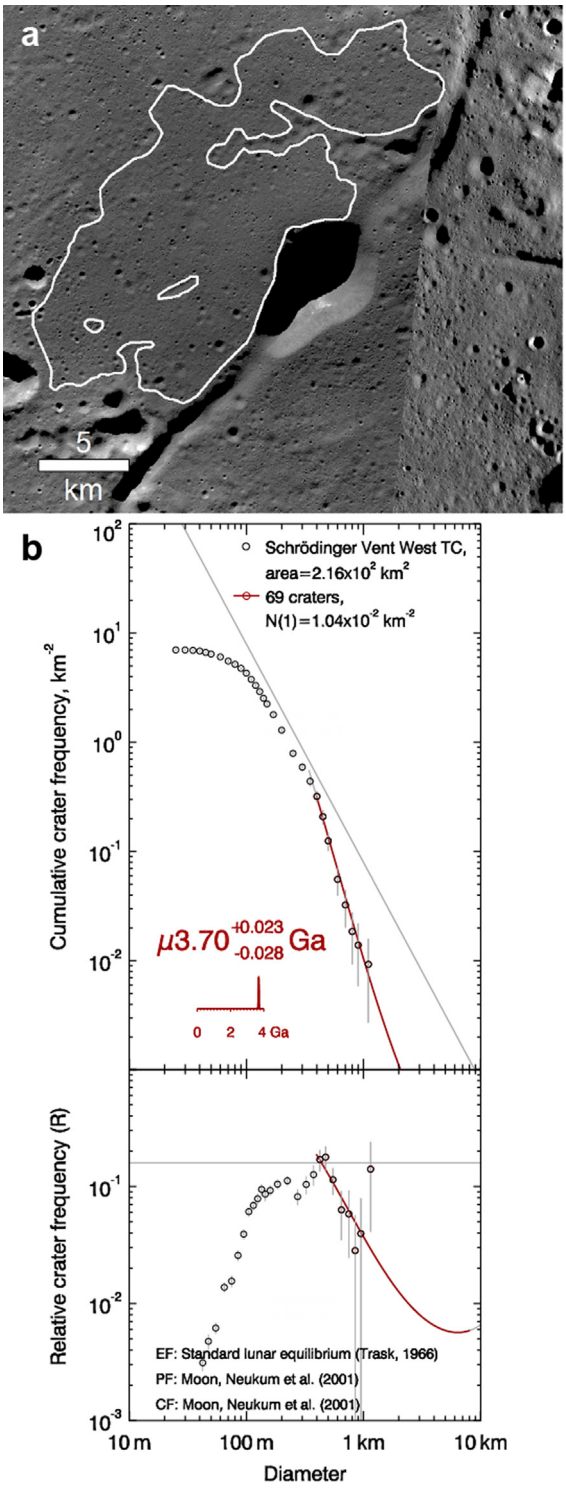

Fig. 2. (a) Count area on the pyroclastic deposit adjacent to a volcanic vent in Schrödinger basin used to determine an absolute model age via a crater size-frequency distribution (CSFD) measurement as seen in the SELENE Terrain Camera seamless orthomosaic (~7 m/px resolution). Areas affected by obvious secondary craters were excluded. (b) The fit of the CSFD gives an absolute model age of ~ 3.70 Ga for the surface of the vent area, representative of the last significant volcanic activity.

25 m contour increments. The margin of the pyroclastic deposit was mapped using Lunar Reconnaissance Orbiter Camera (LROC) data (Kramer et al, 2013). Within those contraints, the volume of pyroclastic material was calculated using a 3D model derived from SLDEM2015, which has a resolution of 60 m/pixel. The vent has the morphological characteristics of a pyroclastic vent. Pyroclastic glasses sampled by Apollo missions have particle diameters generally < 1 mm (e.g., Arndt et al., 1984). Thus, we do not anticipiate particle sizes in the vent would invalidate the method by exceeding the countour interval. Uncertainties inherent in the calculation are related to the uncertainties in the SLDEM2015 data, which are < 10 m horizontally and < 1 m vertically.

Vented volatiles. The abundances of CO_2, H_2O, F, S, and Cl were determined in very-low-Ti and low-Ti pyroclastic glasses from Apollo 15 (15427,41) and high-Ti pyroclastic glasses from Apollo 17 (74220,864) (Saal et al., 2008). Diffusive degassing models were then used to infer original magmatic volatile abundances. In a complementary study, the abundances of H_2O, F, S, and Cl were measured in melt inclusions trapped in olivine within pyroclastic glass spherules from the same Apollo 17 sample (Hauri et al., 2011). The goal was to measure directly the volatile abundances that existed in the magma prior to any degassing. In addition, models of the fire-fountain eruptive process that produced the Apollo 17 glass provide an independent estimate of the CO and CO_2 that was liberated (Rutherford and Papale, 2009). In a first set of calculations presented here, the CO and CO_2 abundances of Rutherford and Papale (2009) are used. The H_2O, F, S, and Cl abundances determined by Hauri and others (2011) are generally lower than those of Saal and others (2008) and are used in this first set of calculations to be conservative in estimates of degassed volatile mass. We note that the degassing of volatile components is not equal – a larger fraction of the CO and CO_2 (100%) and H_2O (98%) species were lost compared to that of F (45%), S (19%), and Cl (57%) (Saal et al., 2008; Hauri et al., 2011; Rutherford and Papale, 2009).

The results of Rutherford and Papale (2009), used in the first set of calculations, assumes 90/10 partitioning of C into CO and CO_2. It does not assume any speciation of S, reporting results in bulk S. In a second set of calculuations, we utilize the results of thermodynanmic calculations and experiments as applied to orange glass compositions (Rutherford et al., 2017). In this case, C is partitioned entirely into CO and S is partitioned into SO_2, H_2S and S_2.

Mapping permanentaly shadowed regions. A map of permanent shadows within the Schrödinger basin was generated using the LunarShader software (Bussey et al., 2010; McGovern et al., 2013). LunarShader is a high-fidelity tool that uses ray tracing to produce precise illumination simulations. It uses as input a Digital Elevation Model and a user-selected Sun location. The software outputs a map of illuminated locations on the lunar surface. A user can choose to output either a binary (lit/dark) map or a map where a Lambertian photometric function has been applied so that the output image has a realistic appearance. Mapping permanent darkness is achieved by producing a simu-

lation in 1/4° subsolar increments – thus a total of 1440 positions – with subsolar latitude of -1.588°, which represents the most southerly position of the Sun and, thus, the highest point in the sky for a location in the southern hemisphere.

Modeling transport and deposition of volatiles. A model was developed to simulate the migration by following a large number of test particles on successive hops through the Moon's exosphere until they are ultimately lost from the system. Each molecular species can be simulated separately using migration and trapping parameters specific to the species. The transport calculations used a Monte Carlo model that follows particles along their trajectories through the lunar exosphere using the equation of motion due to gravity (Crider and Vondrak, 2000; Hurley, 2011). Particles were launched from the Schrödinger vent with a velocity taken from a Maxwell-Boltzmann distribution at temperature 500 K, using the species in the first calculation of vented volatiles. Runs were also conducted for T = 250 K, 750 K, and 1000 K with similar trapping statistics, using the species in the first calculation of vented volatile mass. The code calculates a sticking time for any particle that encounters the surface to determine the time and position of re-release into the exosphere with a velocity chosen from a Maxwell-Boltzmann distribution at the local surface temperature (Hurley et al., 2015). Loss processes included are photodissociation using rates from Huebner and others (1992), escape using the Hill sphere as the upper boundary of the simulation space, and trapping on the surface of the Moon. Trapping schemes were varied based on molecular species. The area of the cold traps was scaled based on Diviner temperature data (Paige et al., 2010) and the assumed stability temperature (Zhang and Paige, 2009).

3. Results

3.1. Age of vent and timing of venting volatiles

Of the craters measured in the 2.16×10^2 km^2 count area (Fig. 2a), those $\geq$ 400 m (n = 69) could be fit with the lunar production function and give an absolute model age of 3.70 $^{+0.02}_{-0.03}$ Ga using Poisson timing analysis (Fig. 2b). Thus, our result places the end of vent activity at the beginning of the Upper Imbrian period. Our result is consistent with the Wilhelms et al. (1979) map that place the dark mantling material in the Imbrian period. Shoemaker and others (1994) later estimated the vent to be 1 to 2 billion years old (late Eratosthenian) based on Clementine high-resolution data. However, their work relied on an examination of the diameter at and below which small craters are in equilibrium, and translation of this value to an estimated age, rather than the use of a lunar cratering chronology. A similar approach also produced estimated ages for the Taurus Littrow pyroclastics that were dramatically younger than the radiometric ages returned by the Apollo 17 mission – a discrepancy that was interpreted to stem from the higher rate of degradation of pyroclastic versus mare units (Lucchitta and Sanchez, 1975; van der Bogert et al., 2016). More recently, Mest (2011) estimated the vent to be 3.7 to 2.5 billion years old (Upper Imbrian to middle Eratosthenian) via analysis of the relative ages of geological units defined in his geological map. His work used the Hartmann chronology (e.g., Hartmann et al., 2000; Hartmann and Neukum, 2001), and bracketed the age of the vent based on stratigraphic relationships, rather than reporting specific absolute model age results. We determined a refined and more precise age by applying the lunar cratering chronology to derive an absolute model age for the CSFD measured in our carefully defined count area (Fig. 2). The robustness of the age determination is supported by work showing that an absolute model age determined on the pyroclastic deposits northwest of Taurus Littrow valley is similar to the radioisotopic age of orange glass sampled at the Apollo 17 landing site (van der Bogert et al., 2016). In addition, our derived age for the vent is consistent with the relative and absolute ages determined for other surrounding units and the basin itself (Wilhelms et al., 1979; van der Bogert et al., 2021).

Because the determined absolute model age represents the end of the deposition of pyroclastic materials, the accompanying volatiles could be sequestered in PSRs that are approximately this age and older. Tye et al. (2015, 4 craters) and Deutsch et al. (2020, additional 20 craters) investigated the ages of craters in the south polar region. Based on our results, craters that show evidence for surface water ice and could host volatiles from the Schrödinger vent would include those > 3.7 Ga in age, namely Haworth (4.18 $^{+0.02}_{-0.02}$ Ga), Shoemaker (4.15 $^{+0.02}_{-0.02}$ Ga), Faustini (4.10 $^{+0.03}_{-0.03}$ Ga), Deutsch et al.'s unnamed crater 1 (3.9$^{+0.1}_{-0.1}$ Ga), Cabeus B (3.9 $^{+0.1}_{-0.1}$ Ga), de Gerlache (3.9 $^{+0.1}_{-0.1}$ Ga), Nobile (3.8 $^{+0.1}_{-0.1}$ Ga), Slater (3.8 $^{+0.1}_{-0.1}$ Ga), Scott (3.8 $^{+0.1}_{-0.1}$ Ga), Sverdrup (3.8 $^{+0.1}_{-0.1}$ Ga), and Deutsch et al.'s unnamed crater 2 (3.7 $^{+0.1}_{-0.1}$ Ga). We note that Li et al. (2018) detected surface water ice at all of these craters.

To make a direct comparison between our age determination for the vent and select craters in the region, we refit two of the CSFD datasets collected by Tye et al. (2015) using Poisson timing analysis for display alongside our CSFD of the vent (Fig. 3). Poisson timing analysis provides improved fitting and error analysis through application of probability functions, in contrast with the cumulative fit approach (Michael et al., 2016). First, we updated the age determination for Faustini crater, since it is the second youngest of the craters analyzed by Tye et al. (2015), and get the same result as in their work (Fig. 3). For Shackleton crater (Fig. 3), we determined an updated age of 3.43 $^{+0.04}_{-0.05}$ Ga, which is slightly younger than the age (3.51 $^{+0.05}_{-0.08}$) of Tye et al. (2015). Thus, Shackleton crater would not have been a catchement for Schrödinger vent volatiles. However, numerous other polar craters could have acted as volatile sinks.

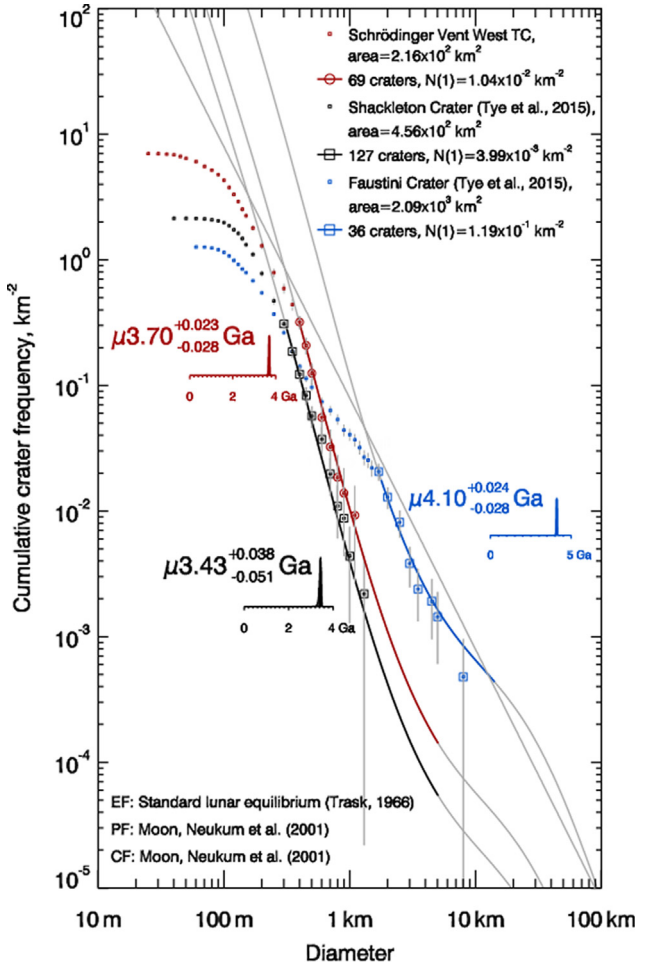

Fig. 3. A comparison of the absolute model ages of the Schrödinger vent and Shackleton and Faustini craters at and near the south pole. The latter two ages were updated by applying the Poisson fitting method of Michael et al. (2016) to the Tye et al. (2015) datasets.

3.2. Abundances of vented volatiles

Using the values of Rutherford and Papale (2009) and Hauri et al. (2011), corresponding minimum to maximum abundances liberated per erupted mass are 105 to 1050 ppm for CO, 18 to 183 ppm for CO_2, 77 to 401 ppm for H_2O, 3 to 12 ppm for F, 36 to 67 ppm for S, and 0 to 0.6 ppm for Cl. The bulk density of a primary pyroclastic unit is taken to be 2.04 g/cm^3, which is the measured value in a portion of Apollo sample 74002 (Mitchell et al., 1973). This sample is the upper part of a drive tube through orange soil that is adjacent to the soil clod sample 74220 used in the analyses of volatile abundances (Saal et al., 2008; Hauri et al., 2011; Rutherford and Papale, 2009). Sample 74220 is 92.3 to 95.9% glass (Heiken and McKay, 1974), while the top of 74002 is 91.2% glass and the 90 to 150 μm fraction is 99.9% glass (McKay et al., 1978). Thus, it is representative of an uncontaminated pyroclastic deposit like that at Schrödinger.

Multiplying the bulk density times the volume of a pyroclastic deposit produces an estimate of the mass of spherules. Using the volatile abundances and degassing fractions described above, one then derives the mass of volatiles degassed as shown in Fig. 4. These volumes are substantial, but also represent lower limits of the contribution of volcanically-produced gases to the lunar exosphere and regolith.

The Schrödinger vent has a Lunar Orbiter Laser Altimeter (LOLA)-derived volume of ~190 km^3 (Fig. 5), corresponding to the level of abundances shown in Fig. 4. The degassed minimum to maximum masses are explicitly: $H_2O = 3.0 \times 10^{13}$ to 1.6×10^{14} g; $CO = 4.1 \times 10^{13}$ to 4.1×10^{14} g; $CO_2 = 7.0 \times 10^{12}$ to 7.1×10^{13} g; $F = 1.2 \times 10^{12}$ to 4.6×10^{12} g; $S = 1.4 \times 10^{13}$ to 2.6×10^{13} g; and $Cl = 0$ to 2.2×10^{11} g. These values are substantial. The mass of water, for example, is 12,000 to 62,000 times larger than that in an Olympic-size pool. It is important to note that the molecular form of the vented H-O species is still uncertain (Robinson and Taylor, 2014). While it is often described as being water (Saal et al., 2008; Hauri et al., 2011), the vented species may have a more reduced form. For that reason, in the volatile transport calculations below, we also model the degassed water in the form of OH.

Using, instead, the results of thermodynamic calculations and experiments as applied to orange glass compositions (Rutherford et al., 2017), C is partitioned entirely into CO and S is partitioned into SO_2, H_2S and S_2. In this case, the corresponding minimum to maximum abundances liberated per erupted mass are 12 to 1395 ppm for CO, 801 to 923 ppm for H_2O, 200 to 234 ppm for SO_2, 100 to 149 ppm for H_2S, 0 to 118 ppm for S_2, 30 to 50 ppm for F, and 1.2 to 1.8 ppm for Cl. The bulk density of a primary pyroclastic unit is taken, again, to be 2.04 g/cm^3, which is the measured value in a portion of orange glass sample 74002 (Mitchell et al., 1973).

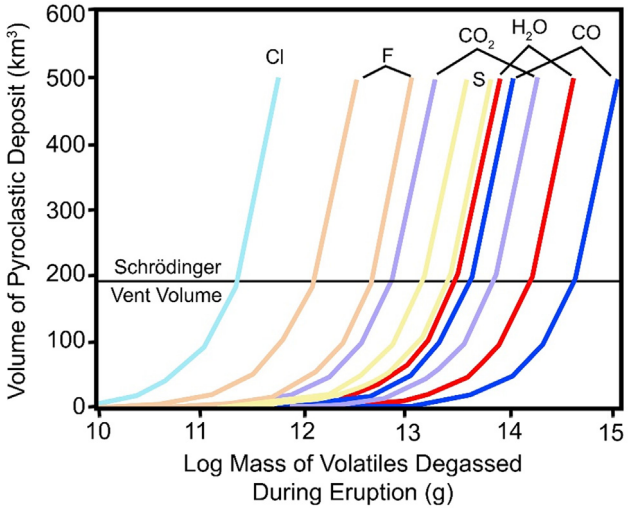

Fig. 4. Minimum and maximum mass of volatiles degassed during eruptions producing pyroclastic deposits with volumes up to 500 km^3. A single curve for Cl represents maximum values; the minimum is zero. The volume of the Schrödinger vent (see Fig. 5) and the correlated mass of volatiles degassed are shown along a horizontal line.

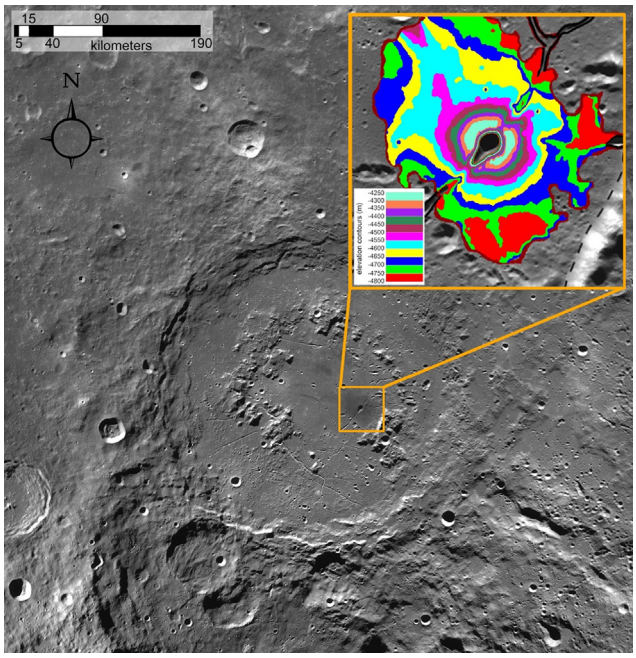

Fig. 5. The vent on the floor of the Schrödinger basin and (inset) LOLA-derived topographical contours of the vent deposit in increments of 25 m that represent a total eruptive volume of ~ 190 km^3.

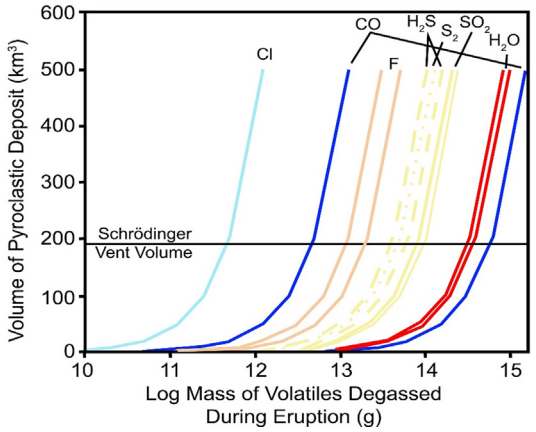

Fig. 6. Minimum and maximum mass of volatiles degassed during eruptions producing pyroclastic deposits with volumes up to 500 km^3. A single curve for Cl represents both the minimum and maximum values. A single curve for S_2 represents maximum values; the minimum is zero. The volume of the Schrödinger vent (see Fig. 6) and the correlated mass of volatiles degassed are shown along a horizontal line.

These paramaters suggest a half-order of magnitude more water was vented (Fig. 6) and sulfur is partitioned into three species that represent slightly more mass, accounting for the addition of H and O to those species. There is more uncertainty in the amount of CO vented, although the maximum estimated value is only slighltly larger than that in the first calculation.

Model calculations suggest typical velocities for a rising dike is of order 30 m/s (Rutherford et al., 2017) and venting material much faster, which is sufficient to account for most of the material in the immediate vicinity of the Schrödinger vent (Fig. 1). Material at the edges of the vent (e.g., 7 km distance) required velocities of 100 to 200 m/s if on ballistic flights with 45 to 80° trajectories that are required for material to clear the walls of the vent's crater and land on the flanks of the cone.

3.3. Cold traps within Schrödinger basin

Some of the volatiles may be trapped within cavities in Schrödinger (e.g., lava tubes, crevices in the impact units, and the interior of the vent itself) that are being detected by extensive geologic analyses of the Schrödinger basin (O'Sullivan et al., 2011; Kramer et al., 2013; Kumar et al., 2013; Kumar et al., 2016). In addition, illumination analyses indicate the vent, portions of a nearby crater floor fracture, and two simple craters are in permanent shadow where volatiles can be incorporated into regolith (Fig. 7). Thus, there may be ice-rich deposits within the Schrödinger basin that could be analyzed and utilized by future lunar surface missions.

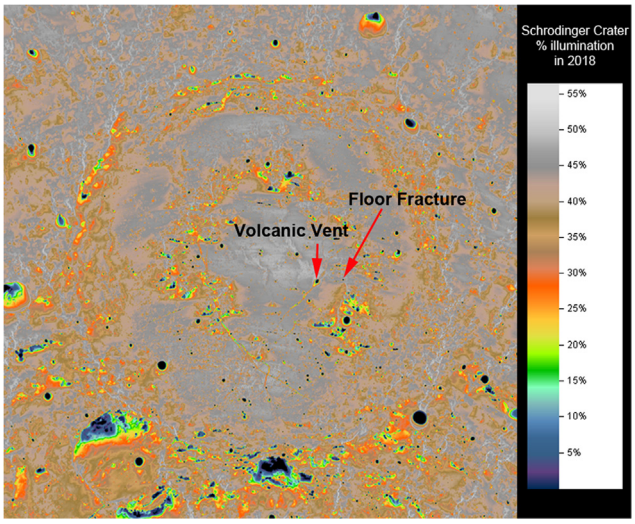

Fig. 7. Map of permanently shadowed regions (appearing black) that currently exist within Schrödinger basin.

3.4. Transport of volatiles to the lunar north and south poles

The Schrödinger vent occurs ~ 500 km from the lunar south pole. There will be a strong tendency for the volatiles to migrate towards the pole (Watson et al., 1961; Arnold, 1979). The latitude or proximity of a volatile source to a pole affects the probability of trapping (e.g., Butler, 1997). Volatiles migrate on a random walk. They are equally probable of moving in any direction from Schrödinger. However, the particles that move poleward are more likely to stick, thus ending their journey. The particles that move poleward that do not stick will have a lower temperature for their next hop, which produces a reduced hop length for their next hop. That makes it more probable they will stay local in the polar region.

Although Shoemaker and others (1994) suggested the vent erupted <2 billion years ago, while the Moon was in the current orbital/spin configuration, implying any volatiles released would have been transported to the current poles, our work (Section 3.1) suggests an older age. In either case, it is important for the transport of those volatiles to be modeled and predictions made for abundances en route, so that future measurements can be used to test transport mechanisms. The model simulates the migration by following a large number of test particles on successive hops through the Moon's exosphere until they are ultimately lost from the system. Each molecular species can be simulated separately using migration and trapping parameters specific to the species.

We used the Diviner maximum temperature maps (Williams et al., 2017) to determine the total area with a maximum temperature <60 K (the rough stability temperature of CO_2) and compared that to total area with maximum temperature <110 K (the rough stability temperature of H_2O). The ratio is 7%. We combined that with an estimate (Mazarico et al., 2011) of the area in permanent shadow, 20,000 km^2, which may provide a better estimate of the area available for trapping water, because it allows for more small size scale cold traps. Applying 7% to that value, we obtain 1400 km^2 of area available for trapping CO_2. Large quantities of CO_2 are retained, even assuming that CO_2 can only stick on about 7% of the surface area that water can stick to.

The calculations indicate 21%, or 8×10^9 kg, of CO_2 will be deposited in the south polar region (Table 1). Dry ice trapping begins 10° from the pole, but most trapping is within 5° of the pole. Water trapping begins 20° from the pole, but most trapping is within 5° of the pole; i.e., within the Artemis exploration zone that extends 6° from the pole. Smaller mass (i.e., 1.2×10^9 kg CO_2) will reach the north pole. The significant transport and deposition of CO_2 is due to both the higher mass and longer lifetime against photodissociation than water. The higher mass helps because it inhibits the mobility of CO_2; i.e., CO_2 does not spread out from the source region as fast. Mobility is governed by an effective velocity that describes the random walk of particles from the source. On an individual hop, a CO_2 molecule has a lower velocity than an H_2O molecule originating from the same spot, because the thermal velocity is proportional to $m^{-1/2}$. With CO_2 at m = 44 amu and H_2O at m = 18 amu, the thermal velocity of CO_2 is 64% of the thermal velocity of H_2O. That translates into a shorter hop length for CO_2 compared with that of H_2O and a lower effective velocity.

In addition, CO_2 has a relatively short residence time adsorbed to the lunar surface on the night side, because the surface temperature is often above the sticking temperature and, thus, CO_2 is rereleased immediately. If the surface is below the sticking temperature, CO_2 particles will stick on the surface until the Moon rotates to a place where the surface temperature exceeds the sticking temperature. If the residence times are short compared with the time it takes the Moon to rotate to a different thermal regime, we can assume they are effectively zero. Thus, much of the migration occurs without being subject to photodissociation, effectively increasing the lifetime of CO_2 in the lunar exosphere. In contrast, CO is lost because there is only a very small fraction of surface area where CO is stable over long times.

For that reason, if the vented C-species is entirely CO as assumed for the second calculation, volcanic venting would produce little dry ice deposition in the polar regions. Observations of CO_2 in the LCROSS experiment (Colaprete et al., 2010) suggest the parameters in the first calculation are correct, if volcanic venting, like that in Schrödinger, is responsible for the type of deposit in Cabeus. We note that the observation of H_2S and SO_2 in that experiment (Colaprete et al., 2010) is also consistent with a volcanic source of volatiles. Those observations are inconsistent with the parameters of the second calculation, and/or require a non-volcanic source of the observed CO_2, or require a source of oxygen that converts CO to CO_2 (Aleinov et al., 2021). If CO is converted to CO_2, then more CO_2 will be deposited in the polar regions.

The calculations indicate about 12%, or about 10^{10} kg, of the water will be deposited in the south polar region (Table 1). Water does not last as long as CO_2 based a trade between two processes. First, its photodissociation lifetime is shorter than CO_2 (Huebner et al., 1992); it spends most of its time hopping in sunlight, because of its long residence time adsorbed to the surface on the nightside. That is, all water hops originate in sunlight and water spends nearly 100% of its airborne time in sunlight. The only time that a water molecule would be airborne in darkness would be if it starts on the dayside and its trajectory carries it across the terminator and it lands at night. This is only a very small part of a small number of hops (of order 100 km long) that occur in the Moon's shadow. In contrast, because carbon dioxide can hop on the nightside, it spends significantly less than 100% of its airborne time in sunlight.

Table 1
Masses of vented molecular species trapped in lunar polar regions, percentage of source that is trapped, and percentage relative to water.

Species	North Pole	South Pole
H_2O	4.5×10^8 kg (0.5%) (100%)	1.1×10^{10} kg (12%) (100%)
OH	1.1×10^6 kg (0.003%) (0.24%)	1.4×10^8 kg (0.5%) (1.3%)
CO_2	1.2×10^9 kg (3%) (267%)	8.0×10^9 kg (21%) (73%)
CO	6.8×10^5 kg (0.003%) (0.15%)	8.8×10^7 kg (0.04%) (0.8%)

We note, second, that a greater portion of the surface area is able to trap water for long times (c.f., 20,000 km^2 for H_2O and 1400 km^2 for CO_2), which starts to compensate for the fewer number of hops available for a water molecule to reach a cold trap. The delivery efficiency is, however, still lower than CO_2. As shown in Table 1, only 12% of H_2O is trapped in the south pole, while 21% of CO_2 is trapped. If water is vented as OH rather than H_2O, then trapping in PSRs is still lower than that of CO_2 (Crider and Vondrak, 2003). In that case, only 0.5%, or 1.4×10^8 kg, of the water will be deposited in the south polar region.

As can be seen in Table 1, more volatiles are trapped in the (closer) south polar region than in the north polar region. The asymmetry is greater for water, showing that the loss rate dominates the distribution of water to a greater degree than CO_2. The fraction able to reach the north pole is greater for CO_2, because it takes many more hops and a greater fraction survives long enough to migrate from one hemisphere to the other. Most (>90%) of the vent volatiles are trapped within 2 months. For an impact gardening of ~ 1 mm/Myr (Arnold, 1979), the volatiles could be buried 1 to 4 m below the surface, depending on the age of eruption, and assuming impact gardening dominates the redistribution with depth compared to thermal diffusion in the coldest PSRs.

Volcanic venting, having a lower temperature than the delivery of exogenous volatiles during an impact event, is a fairly efficient means of delivering volatiles to cold traps. There is very little thermal escape from venting compared to an asteroid or comet impact. Temperatures associated with asteroid and comet impacts are several 1000 K, compared to volcanic vents at ~ 500 K. The thermal velocity is proportional to the square root of temperature, so that is a factor of 3 difference between a vent and an impact source. For CO_2, 0% of particles exceed V_{escape} for a thermal distribution at T = 500 K, whereas 20% exceed V_{escape} for a thermal distribution at T = 5000 K. For water the numbers are 65% at 5000 K and $\ll$1% at 500 K.

4. Discussion and Conclusions

The results in Figs. 5 and 7 utilized the calculated volatile abundances in melt that was pyroclastically lofted to produce Apollo 15 green glass. Those calculated volatile abundances were derived from a diffusion model using a cooling rate of 2 °C/s for 300 s before quenching (Saal et al. 2008). A 2 °C/s cooling rate is consistent with the cooling rate of melt droplets being slowed within a warm eruptive cloud, as suggested by olivine morphology (Arndt et al., 1984) and chemical gradients in glass adjacent to olivine (Kring and McKay, 1984), rather than cooling radiatively to space. Recently, Zhang et al. (2019) reexamined the Saal et al. (2008) glass measurements with new water diffusivity values and suggested a slightly modified cooling rate of 1 to 2 °C/s for 600 s fit data better than cooling for only 60 s. Potentially, a slightly lower cooling rate for longer time can affect calculated melt volatile abundances and fractional volatile loss.

While the vent may have been an important source of volatiles deposited in PSRs within the Schrödinger basin and the south polar region, we do not anticipate significant amounts of water within pyroclastic glass around the vent. Analyses of M^3 spectra (Kramer et al., 2015) indicate the pyroclastic material has weaker OH absorption bands than do other lithologies within the Schrödinger basin (cf., Milliken and Li, 2017; Bandfield et al., 2018). Moreover, a parasitic impact crater in the pyroclastic vent that exposes relatively fresh subsurface pyroclastic material has even weaker OH absorption bands. Thus, the melt seems to have very efficiently lost water during eruption, consistent with the 98% loss rate inferred in Section 2.

On the other hand, lunar pyroclastic glasses are known to have surfaces that are enriched in other volatiles like S, Ag, Cd, Zn, and Br (Quaide and Oberbeck, 1975; Baedeker et al., 1974; Chou et al., 1975) by factors of 3 to 400 compared to their interiors. That suggests modest chemical etching or abrasion may remove them for ISRU (Wasson et al., 1976). Because such pyroclastic deposits are fine-grained, easily excavated, transported, and processed, they have been an attractive target for those volatiles and building materials needed for a sustainable exploration program.

Collectively, the results presented here and those from prior studies of lunar pyroclastic materials, indicate missions to the Schrödinger basin that were initially designed to evaluate the lunar magma ocean and lunar cataclysm hypotheses (O'Sullivan et al., 2011; Burns et al., 2013; Potts et al., 2015; Steenstra et al., 2016) may simultaneously be able to address some of the exploration (ISRU) issues relevant to NASA's Human Exploration and Operations Mission Directorate (HEOMD). Indeed, the immense pyroclastic deposit in Schrödinger, coupled with potential volatile deposits, further enhances Schrödinger as an exploration target. If samples of the pyroclastic vent are collected and the age of the eruption measured, then a precise length of time for the transport and deposition of the volatiles over the lunar surface will be constrained.

Vents like the one in the Schrödinger basin produced H_2O and $CO + CO_2$ masses at the lunar surface on the order of 10^{12} to 10^{15} g for pyroclastic volumes of 10 to 500 km^3. These substantial masses are presented with the caveat that they are based on data inferred mostly from Apollo 15 and 17 materials. Those materials are considered good proxies for several reasons. They represent a broad range of basalt compositions (Saal et al., 2008; Hauri et al., 2011), from very-low Ti to high-Ti basalt, so they bracket the basalt composition of Schrödinger (Gaddis et al., 2003). The Hadley Cleft pyroclastic deposit of Apollo 15 covers an area similar to that of the Schrödinger deposit (Gaddis et al., 2003). And there is no evidence for an increase or decrease in volatile content in lunar basalts (Robinson and Taylor, 2014) with the eruption age of those basalts. Nonetheless, samples of additional vent material,

like that at the Schrödinger basin (O'Sullivan et al., 2011; Bunte et al., 2011; Potts et al., 2015; Steenstra et al., 2016), need to be returned to Earth to verify the Apollo 15 and 17 values are valid for other lunar pyroclastic vents.

There is a hint that the Schrödinger pyroclastic material has a major element composition distinct from that of either green or orange glass of Apollo. Orbital spectra of Schrödinger pyroclastic material (Kobayashi et al., 2010; Kramer et al., 2013) indicate TiO_2 abundances are very low. Significant quantities of ilmenite are not indicated by that data and, thus, may not be available for hydrogen reduction (Duke et al., 2006) to produce oxygen (Hawke et al., 1990). One would, instead, have to rely on carbothermal ISRU processes for the production of water. Those same spectra (Kramer et al., 2013) indicate that FeO is 10 to 14 wt% in Schrödinger pyroclastic material, which is substantially less than that of both orange (~23 wt% FeO) and green (~20 wt% FeO) glass (Arndt et al., 1984, 1987). The glass appears to coexist with orthopyroxene (Shankar et al., 2013; McBride et al., 2019), rather than the olivine that characterizes green and orange glasses in the Apollo collection. It is not yet clear if these differences represent a nearside-farside dichotomy in mantle-derived pyroclastic source regions or a significantly different source depth for Schrödinger pyroclastic melt relative to those of Apollo pyroclastic glasses. Again, samples may need to be returned to Earth to further evaluate the chemistry of those magmatic products and their implications for lunar evolution and a globally expanded assessment of magmatic sources of volatile constituents.

The Schrödinger vent may be one of the largest sources of indigenous volatiles in the south polar region. The total volume of water in the polar permanently shadowed regions is estimated to be a few times 10^{11} kg (Eke et al., 2009). The volume of water released by the Schrödinger vent is a few percent to several tens of percent of that water. Loss mechanisms reduce the mass of Schrödinger volatiles deposited, but that vent is still likely to be responsible for 3 to 6 % of the total water estimated to be in lunar PSRs. If the Schrödinger vent tapped the same type of mantle water seen in Apollo samples, then that source of water will have hydrogen and nitrogen isotope compositions derived from a mantle source dominated by contributions from asteroids rather than comets (Barnes et al., 2016), although fractionation processes as the volatiles are transported across the surface may alter isotopic signatures.

The volatiles appear to have been vented until ~ 3.7 Ga and, thus, may have been deposited in several older polar craters (e.g., Haworth, Shoemaker, Faustini, de Gerlache, Nobile, Slater, Scott, Henson, and Sverdrup in the south polar region), but not Shackleton crater, because it did not yet exist. The Schrödinger vent volatiles may be one of the sources that produced an observed displacement of maximum H concentrations from current pole locations (Siegler et al., 2016). If one of the lunar sample return missions being developed (O'Sullivan et al., 2011; Bunte et al., 2011; Burns et al., 2013; Potts et al., 2015; Steenstra et al., 2016) for the Schrödinger basin is flown, samples of the pyroclastic vent are collected, and the age of the eruption measured, then the Schrödinger vent's contribution to polar volatiles will be better constrained.

Venting like that in Schrödinger would episodically replace the normal surface boundary exosphere with a transient, conventional collisional atmosphere, although it would be quite thin (e.g., Stern, 1999). Using the method developed above to evaluate the Schrödinger vent volume and, thus, volatile production mass, one can calculate mass production rates for the other ~ 100 vents observed on the Moon and, using mare volumes, produce a similar set of volatile production masses. Integrating those calculations with mare and vent ages (Needham and Kring, 2017), one can derive a production rate function for volatiles throughout lunar history. Thus, the results described here provide a foundation for a global assessment of volcanic degassing contributions to the evolution of the lunar atmosphere and subsequent deposition of those volatiles in PSRs.

Declaration of Competing Interest

The authors declare that they have no known competing financial interests or personal relationships that could have appeared to influence the work reported in this paper.

Acknowledgements

Geologic assessment of the volcanic vent in Schrödinger basin was supported by the NASA Lunar Science Institute (NLSI) through a Cooperative Agreement with the Lunar and Planetary Institute (LPI) (NNA09DV33A, Principal Investigator DAK). Calculations of volatile production were supported by the NASA Solar System Exploration Research Virtual Institute (SSERVI) through cooperative agreements with the LPI (NNA14AB07A and 80NSSC20M0016, PI DAK). The LunarShader illumination-simulation capability was developed at JHU/APL, partly funded by NLSI (contract NNA09DB31A, PI DBJB) and SSERVI (contract NNA14AB02A, PI DBJB). Calculations of volatile transport was supported by the SSERVI VORTICES Institute (contract NNA14AB02A, PIs DBJB and Andrew S. Rivkin). CSFD measurements (CHvdB) were supported by German Aerospace Center (Deutsches Zentrum für Luft- and Raumfahrt) projects 50OW1504 and 50OW2001. We thank two anonymous reviewers for helpful comments and Associate Editor Ernesto Palomba for handling the manuscript. LPI Contrib. No. 2640.

References

Aleinov, I., Way, M.J., Tsigaridis, K., Wolf, E.T., Harman, C., Gronoff, G., Hamilton, C.W., 2021. The rold of the transient volcanically-induced lunar atmosphere in transport and deposition of polar volatiles. Lunar Planet. Sci. LII, Abstract #2335.

Allender, E.J., Orgel, C., Almeida, N.V., Cook, J., Ende, J.J., Kamps, O., Mazrouei, S., Slezak, T.J., Soini, A.-J., Kring, D.A., 2019. Traverses for the ISECG-GER design reference mission for humans on the lunar surface. Advances in Space Research 63, 692–727.

Arnold, J.T., 1979. Ice in the lunar polar regions. J. Geophys. Res. 84, 5659–5668.

Arndt, J., von Engelhardt, W., Gonzalez-Cabeza, I., Meier, B. 1984. Formation of Apollo 15 green glass beads. Proc. 15th Lunar Planet. Sci. Conf., Part 1, J. Geophys. Res. 89, C225-C232.

Baedeker, P.A., Chou, C.-L., Wasson, J. T., 1974. The extralunar component in lunar soils and breccias. Proc. 5th Lunar Sci. Conf., 1625-1643.

Bandfield L., J., Poston J., M., Klima L., R., Edwards S., C., 2018. Widespread distribution of OH/H_2O on the lunar surface inferred from spectral data. Nature Geoscience 11, 173–177.

Barnes, J.J., Kring, D.A., Tartèse, R., Franchi, I.A., Anand, M., Russell, S.S., 2016. An asteroidal origin for water in the Moon. Nat. Commun. 7, 11684. https://doi.org/10.1038/ncomms11684.

Basilevsky, A. T., 1976. On the evolution rate of small lunar craters. Proc. 7th Lunar Sci. Conf., 1005-1020

Bunte, M.K., Porter, S., Robinson, M.S., 2011. A sortie mission to Schrödinger basin as reconnaissance for future exploration. Geol. Soc. Am. Sp. Pap. 483, 533–546.

Burns, J.O. et al., 2013. A lunar L2-farside exploration and science mission concept with the Orion Multi-Purpose Crew Vehicle and a teleoperated lander/rover. Adv. Space Res. 52, 306–320.

Bussey, D.B.J. et al., 2010. Illumination conditions of the south pole of the Moon derived using Kaguya topography. Icarus 208, 558–564.

Butler, B.J., 1997. The migration of volatiles on the surfaces of Mercury and the Moon. J. Geophys. Res. 102, 19283–19291.

Chou, C.-L., Boynton, W.V., Sundberg, L.L., Wasson, J.T., 1975. Volatiles on the surface of Apollo 15 green glass and trace-element distributions among Apollo 15 soils. Proc.6th Lunar Sci. Conf., 1701-1727.

Colaprete, A., Schultz, P., Heldmann, J., Wooden, D., Shirley, M., Ennico, K., Hermalyn, B., Marshall, W., Ricco, A., Elphic, R.C., Goldstein, D., Summy, D., Bart, G.D., Asphaug, E., Korycansky, D., Landis, D., Sollitt, L., 2010. Detection of water in the LCROSS ejecta plume. Science 330, 463–468.

Crider, D.H., Vondrak, R.R., 2000. The solar wind as a possible source of lunar polar hydrogen deposits. J. Geophys. Res. 105, 26773–26782.

Crider, D.H., Vondrak, R.R., 2003. Space weathering effects on lunar cold trap deposits. J. Geophys. Res. 108, E7, 5079, 11p.

Deutsch, A.N., Head, J. W. III, Neumann, G.A., 2020. Analyzing the ages of south polar craters on the Moon: Implications for sources and evolution of surface water ice. Icarus 336, doi.org/10.1016/j.icarus.2019.113455.

Duke, M.B., Gaddis, L.R., Taylor, G.J., Schmitt, H.H., 2006. Development of the Moon. Rev. Mineral. & Geochem. 60, 597–656.

Eke, V.R., Teodoro, L.F.A., Elphic, R.C., 2009. The spatial distribution of polar hydrogen deposits on the Moon. Icarus 200, 12–18.

Gaddis, L.R., Staid, M.I., Tyburczy, J.A., Hawke, B.R., Petro, N.E., 2003. Compositional analyses of lunar pyroclastic deposits. Icarus 161, 262–280.

Hartmann, W.K., Neukum, G., 2001. Cratering chronology and evolution of Mars. Space Sci. Rev. 96, 165–194.

Hartmann, W.K., Ryder, G., Dones, L., Grinspoon, D.H., 2000. The time-dependent intense bombardment of the primordial Earth-Moon system. In: Righter, R.M., Canup, R. (Eds.), Origin of the Earth and Moon: Tucson. University of Arizona Press, pp. 493–512.

Haruyama, J., Matsunaga, T., Ohtake, M., Morota, T., Honda, C., Yokota, Y., Torii, M., Ogawa, Y., LISM Working Group, 2008. Global lunar-surface mapping experiment using the Lunar Imager/Spectrometer on SELENE. Earth Planets Space 60, 243-255.

Haskin, L.A., Warren, P., 1991. Lunar chemistry. In Lunar Sourcebook, 357-474, Cambridge University Press.

Hauri, E.H., Weinreich, T., Saal, A.E., Rutherford, M.C., Van Orman, J. A., 2011. High pre-euptive water contents preserved in lunar melt inclusions. Science 333, 213–215.

Hawke, B.R., Coombs, C.R., Clark, B., 1990. Ilmenite-rich pyroclastic deposits: An ideal lunar resource. Proc. 20th Lunar Planet. Sci. Conf, 249–258.

Heiken, G., McKay, D.S., 1974. Petrography of Apollo 17 soils. Proc. 5th Lunar Sci. Conf, 843–860.

Hiesinger, H., Head III, J.W., Wolf, U., Jaumann, R., Neukum, G., 2011. Ages and stratigraphy of lunar mare basalts: A synthesis. Geol. Soc. Am. Special Pap. 477, 1–51.

Huebner, W.F., Keady, J.J., Lyon, S.P., 1992. Solar photo rates for planetary atmospheres and atmospheric pollutants. Astrophys. Space Sci. 195, 1–294.

Hurley, D.M., 2011. Modeling of the vapor release from the LCROSS impact: Parametric dependencies. J. Geophys. Res. 116, E01007.

Hurley, D.M. et al., 2015. An analytic function of lunar surface temperature for exospheric modeling. Icarus 255, 159–163.

Joy, K.H., Visscher, C., Zolensky, M.E., Mikouchi, T., Hagiya, K., Oshumi, K., Kring, D.A., 2015. Identification of magnetite in lunar regolith breccia 60016: Evidence of oxidized conditions at the lunar surface. Meteoritics Planet. Sci. 50, 1157–1172.

Keller, J. W., Petro, N. E., Vondrak, R. R., LRO Team, 2016. The Lunar Reconnaissance Orbiter Mission – Six years of science and exploration of the Moon. Icarus 273, 2-24.

Kneissl, T., van Gasselt, S., Neukum, G., 2011. Map-projection-independent crater size-frequency determination in GIS environments-New software tool for ArcGIS. Planetary and Space Science 59, 1243–1254.

Kobayashi, Y., Ohtake, M., Haruyama, J., Matsunaga, T., Iwata, T., Morota, T., Yokota, Y., Yamamoto, S., Kitazato, K., 2010. Estimating composition of dark mantle deposit in Schrödinger basin using SELENE spectral data. Lunar Planet. Sci. XLI, Abstract #1636.

Krähenbühl, U., Ganapathy, R., Morgan, J. W., Anders, E. (1973) Volatile elements in Apollo 16 samples: Implications for highland volcanism and accretion history of the Moon. Proc. 4th Lunar Science Conf., 1325–1348.

Kramer, G.Y., Kring, D.A., Nahm, A.L., Pieters, C.M., 2013. Spectral and photogeologic mapping of Schrödinger basin and implications for post-South Pole-Aitken impact deep subsurface stratigraphy. Icarus 223, 131–148.

Kramer, G.Y., Kring, D.A., McGovern, P.J., Nahm, A.L., Öhman, T., 2015. Compositional and structural characteristics of Schrödinger's basin volcanism. Lunar Planet. Sci. XLVI, Abstract #2829.

Kring, D.A., McKay, G.A., 1984. Chemical gradients in glass adjacent to olivine in experimental charges and Apollo 15 green glass vitrophyres. Lunar Planet. Sci. XV,, 461–462.

Kumar, P.S. et al., 2013. Gullies and landslides on the Moon: Evidence for dry-granular flows. J. Geophys. Res. 118, 206–223.

Kumar, P.S. et al., 2016. Recent shallow moonquakes and impact-triggered boulder falls on the Moon: New insights from the Schrödinger basin. J. Geophys. Res. 121. https://doi.org/10.1002/2015JE004850, 33p.

Li, S. et al., 2018. Direct evidence of surface exposed water ice in the lunar polar regions. PNAS 115, 8907–8912.

Lucchitta, B.K., Sanchez, A.G., 1975. Crater studies in the Apollo 17 region. Proc. 6th Lunar Sci. Conf, 2427–2441.

Mazarico, E., Neumann, G.A., Smith, D.E., Zuber, M.T., Torrence, M. H., 2011. Illumination conditions of the lunar polar regions using LOLA topography. Icarus 211, 1066–1081.

McBride, M. J., Horgan, B. H. N., Gaddis, L. R., Bennet, K. A., 2019. Moon Mineralogy Mapper analysis of volcanic deposits in Schrodinger basin. Lunar Planet. Sci. L, Abstract #1985.

McGovern, J.A. et al., 2013. Mapping and characterization of non-polar permanent shadows on the lunar surface. Icarus 223, 566–581.

McKay, D.S., Heiken, G.H., Waits, G.A., 1978. Core 74001/2: Grain size and petrology as a key to the rate of in situ reworking and lateral transport on the lunar surface. Proc. 9th Lunar Planet. Sci. Conf., 1913-1932.

Mest, S.C., 2011. The geology of Schrödinger basin: Insights from post-Lunar Orbiter data. Geol. Soc. Am. Sp. Pap. 477, 95–115.

Michael, G.G., Kneissel, T., Neesemann, A., 2016. Planetary surface dating from crater size-frequency measurements: Poisson timing analysis. Icarus 277, 279–285.
Milliken, R.E., Li, S., 2017. Remote detection of widespread indigenous water in lunar pyroclastic deposits. Nature Geoscience 10, 561–565.
Mitchell, J.K. et al., 1973. Soil Mechanics. Apollo 17 Preliminary Science Report, NASA SP-330, Chapter 8.
National Research Council, 2007. The Scientific Context for Exploration of the Moon. National Academy Press, Washington D.C..
Needham, D. H., Kring, D. A., 2017. Lunar volcanism produced a transient atmosphere around the ancient Moon. Earth Planet. Sci. Letters 478, 175-178.
Neukum G., 1983. Meteorite bombardment and dating of planetary surfaces, Translation of: Meteoritenbombardement und Datierung planetarer Oberflächen, Tenure Thesis, Ludwig-Maximilians University, Munich, Germany, NASA Technical Memorandum TM-77558, 153 pp.
Neukum, G., Ivanov, B.A., Wartmann, W.K., 2001. Cratering records in the inner solar system in relation to the lunar reference system. Space Sci. Rev. 96, 55–86.
O'Sullivan, K.M., Kohout, T., Thaisen, K.G., Kring, D.A., 2011. Calibrating several key lunar stratigraphic units representing 4 b.y. of lunar history within Schrödinger basin. In Geol. Soc. Am. Sp. Pap. 477, 117–128.
Paige, D.A. et al., 2010. Diviner lunar radiometer observations of cold traps in the Moon's south polar region. Science 330, 479–482.
Potts, N.J. et al., 2015. Robotic traverse and sample return strategies for a lunar farside misson to the Schrödinger basin. Adv. Space Res. 55, 1241–1254.
Quaide, W., Oberbeck, V., 1975. Development of the mare regolith: some model considerations. The Moon 13, 27–55.
Robinson, K.L., Taylor, G.J., 2014. Heterogeneous distribution of water in the Moon. Nature Geoscience 7, 401–408.
Rutherford, M.J., Papale, P., 2009. Origin of basalt fire-fountain eruptions on Earth versus the Moon. Geology 37, 219–222.
Rutherford, M.J., Head, J.W., Saal, A.E., Hauri, E., Wilson, L., 2017. Model for the origin, ascent, and eruption of lunar picritic magmas. American Mineralogist 102, 2045–2053.
Saal, A.E. et al., 2008. Volatile content of lunar volcanic glass and the presence of water in the Moon's interior. Nature 454, 192–195.
Settle, M., 1979. The structure and emplacement of cinder cone fields. American Journal of Science 279, 1089–1107.
Shankar, B., Osinski, G.R., Antonenko, I., Neish, C.D., 2013. A multispectral geological study of the Schrödinger impact basin. Can. J. Earth Sci. 50, 44–63.
Shaulis, B. J., Kring, D. A., Lapen, T. J., Righter, M. (2016) Petrology and distribution of U-Pb ages in lunar meteorite breccia Miller Range (MIL) 13317. Lunar Planet. Sci. LXVII, Abstract #2027.
Shoemaker, E.M., Robinson, M.S., Eliason, E.M., 1994. The south pole region of the Moon as seen by Clementine. Science 266, 1851–1854.
Siegler, M.A., Miller, R.S., Keane, J.T., Laneuville, M., Paige, D.A., Matsuyama, I., Lawrence, D.J., 2016. Lunar true polar wander inferred from polar hydrogen. Nature 531, 480–484.
Smith, D.E., Zuber, M.Y., Jackson, G.B., Cavanaugh, J.F., Neumann, G. A., Riris, H., Sun, X., Zellar, R.S., Coltharp, C., Connelly, J., Katz, R. B., Kleyner, I., Liiva, P., Matuszeski, A., Mazarico, E.M., McGarry, J. F., Novo-Gradac, A.-M., Ott, M.N., Peters, C., Ramos-Izquierdo, L. A., Ramsey, L., Rowlands, D.D., Schmidt, S., Scott III, V.S., Shaw, G.B., Smith, J.C., Swinski, J.-P., Torrence, M.H., Unger, G., Yu, A. W., Zagwodzki, T.W., 2010. The Lunar Orbiter Laser Altimeter investigation of the Lunar Reconnaissance Orbiter Mission. Space Science Reviews 150, 209–241.
Snape, J.F., Curran, N.M., Whitehouse, M.J., Nemchin, A.A., Joy, K.H., Hopkinson, T., Anand, M., Bellucci, J.J., Kenney, G.G., 2018. Ancient volcanism on the Moon: Insights from Pb isotopes in the MIL 13317 and Kalahari 009 lunar meteorites. Earth Planet. Sci. Letters 501, 84–95.
Sori, M.M., Zuber, M.T., Head, J.W., Kiefer, W.S., 2016. Gravitational search for cryptovolcanism on the Moon: Evidence for large volumes of early igneous activity. Icarus 273, 284–295.
Steenstra, E.S. et al., 2016. Analyses of robotic traverses and sample sites in the Schrödinger basin for the HERACLES human-assisted sample return mission concept. Adv. Space Res. 58, 1050–1065.
Stern, S.A., 1999. The lunar atmosphere: History, status, current problems, and context. Rev. Geophys. 37, 453–491.
Tye, A.R., Fassett, C.I., Head, J.W., Mazarico, E., Basilevsky, A.T., Neumann, G.A., Smith, D.E., Zuber, M.T., 2015. The age of lunar south circumpolar craters Haworth, Shoemaker, Faustini, and Shackleton: implications for regional geology, surface processes, and volatile sequestration. Icarus 255, 70–77.
van der Bogert, C.H., Clark, J.D., Hiesinger, H., Banks, M.E., Watters, T., Robinson, M.S., 2018. How old are lunar lobate scarps? 1. Seismic resetting of crater size-frequency distributions. Icarus 306, 225–242.
van der Bogert, C.H., Gaddis, L., Hiesinger, H., Ivanov, M., Jolliff, B., Mahanti, P., Pasckert, J.H., 2016. Revisiting the CSFDs of the Taurus Littrow dark mantle deposit: Implications for age determinations of pyroclastic deposits. Lunar Planet. Sci. Conf. 47, #1616.
van der Bogert, C. H., Poehler, C. M., Kring, D. A., Hiesinger, H., 2021. Absolute model ages for geological units in Schrödinger basin: Context for the 2024 PRISM CLPS mission. Lunar Planet. Sci. LII, Abstract #2351.
Wasson, J.T., Boynton, W.V., Kallemeyn, G.W., Sundberg, L.L., Wai, C. M., 1976. Volatile compounds released during lunar lava fountaining. Proc. 7th Lunar Sci. Conf., 1583-1595.
Watson, K., Murray, B.C., Brown, H., 1961. The behavior of volatiles on the lunar surface. J. Geophys. Res. 66, 3033–3045.
Whitten, J.L., Head, J.W., 2015. Lunar cryptomaria: Physical constraints, distribution, and implications for ancient volcanism. Icarus 247, 150–171.
Wilhelms E., D., Howard A., K., Wilshire G., H., 1979. Geologic map of the south side of the Moon.,, USGS.
Williams, J.-P., Paige, D.A., Greenhagen, B.T., Sefton-Nash, E., 2017. The global surface temperatures of the Moon as measured by the Diviner Lunar Radiometer experiment. Icarus 283, 300–325.
Zhang, J., Paige, D.A., 2009. Cold-trapped organic compounds at the poles of the Moon and Mercury: Implications for origins. Geophys. Res. Lett. 36, L16203.